Ultra-High Resolution Imaging by Fluorescence Photoactivation Localization Microscopy

Samuel T. Hess,*† Thanu P. K. Girirajan,†‡ and Michael D. Mason†
*Department of Physics and Astronomy, †Institute for Molecular Biophysics, and ‡Department of Chemical and Biological Engineering, University of Maine, Orono, Maine

ABSTRACT Biological structures span many orders of magnitude in size, but far-field visible light microscopy suffers from limited resolution. A new method for fluorescence imaging has been developed that can obtain spatial distributions of large numbers of fluorescent molecules on length scales shorter than the classical diffraction limit. Fluorescence photoactivation localization microscopy (FPALM) analyzes thousands of single fluorophores per acquisition, localizing small numbers of them at a time, at low excitation intensity. To control the number of visible fluorophores in the field of view and ensure that optically active molecules are separated by much more than the width of the point spread function, photoactivatable fluorescent molecules are used, in this case the photoactivatable green fluorescent protein (PA-GFP). For these photoactivatable molecules, the activation rate is controlled by the activation illumination intensity; nonfluorescent inactive molecules are activated by a high-frequency (405-nm) laser and are then fluorescent when excited at a lower frequency. The fluorescence is imaged by a CCD camera, and then the molecules are either reversibly inactivated or irreversibly photobleached to remove them from the field of view. The rate of photobleaching is controlled by the intensity of the laser used to excite the fluorescence, in this case an Ar+ ion laser. Because only a small number of molecules are visible at a given time, their positions can be determined precisely; with only ~100 detected photons per molecule, the localization precision can be as much as 10-fold better than the resolution, depending on background levels. Heterogeneities on length scales of the order of tens of nanometers are observed by FPALM of PA-GFP on glass. FPALM images are compared with images of the same molecules by widefield fluorescence. FPALM images of PA-GFP on a terraced sapphire crystal surface were compared with atomic force microscopy and show that the full width at half-maximum of features ~86 ± 4 nm is significantly better than the expected diffraction-limited optical resolution. The number of fluorescent molecules and their brightness distribution have also been determined using FPALM. This new method suggests a means to address a significant number of biological questions that had previously been limited by microscope resolution.

INTRODUCTION

Although biological structures span many orders of magnitude in length scale (1), resolution in many types of biological light microscopy is limited. The limit on resolution of point sources imposed by the finite size of the diffraction-limited illumination volume in a far-field optical system (2) is quantified by the Rayleigh criterion (3):

$$r_R = 0.61 \times \lambda / NA,$$

where λ is the wavelength of the detected photons and NA is the numerical aperture of the lens system. To adequately visualize structure, most fluorescence imaging methods rely on observation of a large number of molecules simultaneously, which is inherently limited because the distance between observed molecules is much less than r_R. New imaging methods such as 4Pi microscopy (4–9), patterned illumination microscopy (10,11), stimulated emission depletion (STED) microscopy (12–14), and other types of reversible saturable optical fluorescence transition (RESOLFT) microscopies (15) can increase resolution by reducing the size of the observation volume or, correspondingly, by increasing the accessible Fourier space and therefore increasing the number of accessible spatial frequencies. 4Pi microscopy (6,9) provides a significant increase in axial resolution (~100 nm), but its advantages are more difficult to apply toward examination of thick or scattering samples, or lateral molecular distributions such as in biological membranes. Although STED does not rely on image deconvolution as 4Pi and patterned illumination microscopy do, both STED and 4Pi depend on nonlinear excitation under high-intensity pulsed illumination. Furthermore, they typically derive their information from large numbers of molecules observed simultaneously, and therefore may obscure crucial behavior that is only discernable at the single-molecule level. Nonlinear structured illumination microscopy (10) has so far achieved resolution (full width at half-maximum (FWHM) of the point spread function (PSF)) of 50 nm and can in principle be improved further, but is limited by the photobleaching properties of the fluorophore, and uses excitation intensities near saturation, where photobleaching may be more pronounced than at low intensity (10). Near-field scanning optical microscopy is also capable of spatial resolution better than the classical diffraction limit, but is typically used to image surfaces and is difficult to use to image in aqueous

Submitted June 12, 2006, and accepted for publication August 28, 2006.

Address reprint requests to Prof. Samuel T. Hess, Dept. of Physics and Astronomy, University of Maine, Orono, ME 04469. Tel.: 207-581-1036; Fax: 207 581-3410; E-mail: sam.hess@umit.maine.edu.

0006-3495/06/12/4258/15 $2.00

doi: 10.1529/biophysj.106.091116

solution (16). Fluorescence resonance energy transfer can access the molecular length scale, but has a limited range of distances over which it is sensitive and depends on a large number of variables, including molecular orientation and distance, dielectric constant, spectral overlap, and excited-state lifetime (17–19). Other single-molecule methods can resolve multiple fluorescent objects at distances longer than those accessible to fluorescence resonance energy transfer and closer than r_R, but only in limited numbers, and only if a very large number of photons is collected per object (e.g., 10^4 photons to resolve two objects separated by 10 nm) (20). Thus, even the most advanced fluorescence microscopy and spectroscopy methods continue to be limited in their range of accessible length scales.

Fluorescent speckle microscopy (FSM) (21–24) provides an additional means to image subdiffraction objects such as actin and microtubules by localizing single molecules as they intermittently emit fluorescence. FSM also exploits (typically stochastic) intermittency of those single molecules, which allows large numbers of molecules ($>10^5$) to be visualized, but does not allow direct control over the number of fluorescent molecules within the field of view. In FSM, the number of visible particles must be controlled by changing the concentration or density per unit area of the fluorophore-labeled molecules themselves, which in the case of green fluorescent protein (GFP)-transfected cells may not be a trivial proposition, especially if the desired density is low. Instead, in fluorescence photoactivation localization microscopy (FPALM), the number of active fluorophores, as will be explained, can be increased or decreased photophysically by changing the rates of photoactivation and photobleaching, even if the density of fluorophore-labeled molecules is much higher than one fluorophore per μm^2.

We present a novel method by which fluorescence microscopy may be performed to obtain an image with greatly enhanced ability to resolve large numbers of fluorescent molecules. Unlike previous approaches, this method does not suffer from the standard resolution limits because it does not exclusively rely on resolution for visualization of multiple molecules. Rather, single molecules are localized in modest numbers, allowing position localization, which is far more precise than the resolution limit. We demonstrate this principle using photoactivatable green fluorescent protein (PA-GFP) molecules that are initially found in a dark (weakly fluorescent) state, can be either reversibly or irreversibly activated by one excitation wavelength, and then can be visualized by excitation with a second wavelength. A small number of stochastically photoactivated molecules, which are spatially separated from each other (on average) by several times the resolution, are then localized using single-molecule detection methods, in this case a high-quantum efficiency charge-coupled device (see Fig. 1). After a (stochastically determined) number of photons has been collected from the molecule, the readout cycle ends by photobleaching of that particular molecule, and the process is repeated until the total number of localized molecules is very large. The positions of readout (observed and localized) molecules are then tabulated and plotted to construct a two-dimensional map (image). The acquisition of this single-molecule information also permits determination of the fluorescence brightness and mean molecular velocity during the acquisition time.

In principle, this method can be used for any photoactivatable molecular species whose photophysical properties are sufficient under the following five photoactivation excitation and detection conditions.

1. The spontaneous interconversion rates into and out of the activated (fluorescent) state must be low compared to the light-controlled activation rate.
2. For irreversible photoactivation, the photobleaching quantum yield must be finite and, when multiplied by

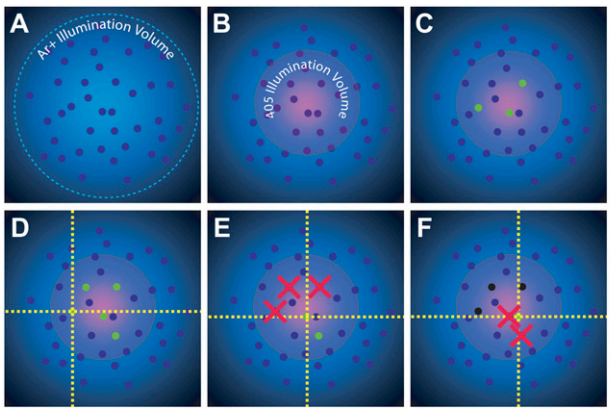

FIGURE 1 Fluorescence photoactivation localization microscopy (FPALM). An area containing photoactivatable molecules (here, PA-GFP) is illuminated simultaneously with two frequencies of light, one for readout (here, an Ar+ ion laser, its spatial illumination profile shown in *A*), and a second one for activation (here, a 405-nm diode laser, its profile superimposed in *B*). Within the region illuminated by the activation beam, inactive PA-GFPs (*small dark blue circles*) are activated (*C*) (*small green circles*) and then localized (*D*). After some time, the active PA-GFPs (*E*) photobleach (*red Xs*) and (*F*) become irreversibly dark (*black circles*). Additional molecules are then activated, localized, and bleached until a sufficient number of molecules have been analyzed to construct an image. (*G*) The experimental geometry shows the 405-nm activation laser (*X405*), which is reflected by a dichroic (*DM1*) to make it collinear with the Ar+ readout laser. A lens (*L1*) in the back port of an inverted fluorescence microscope is used to focus the lasers, which are reflected upward by a second dichroic mirror (*DM2*), onto the back aperture of the objective lens (*OBJ*). The sample, supported by a coverslip (*CS*), emits fluorescence which is collected by the objective, transmitted through DM2, filtered (*F*), and focused by the tube lens (*TL*) to form an image on a camera (*CCD*).

the excitation rate at saturation, must give a photobleaching rate equal to or greater than the activation rate.
3. For reversible photoactivation, the light-controlled deactivation plus photobleaching rate must be equal to or greater than the activation rate.
4. The average number of detected photons per molecule before photobleaching must be large enough to provide the desired resolution enhancement.
5. The fluorescence of the inactive state must be low compared to that of the active state under the given detection conditions; that is, the contrast ratio (25) must be large.

THEORY

The spatial precision of localization of single fluorescent objects has been studied extensively (16,20,26–29). Thompson et al. calculate the localization precision σ_x for point-like objects imaged in two dimensions by fluorescence microscopy to be

$$\sigma_x^2 = \frac{r_0^2 + q^2/12}{N} + \frac{8\pi r_0^4 b^2}{q^2 N^2}, \tag{1}$$

where r_0 is the standard deviation of the point spread function, N is the total number of photons collected, q is the size of an image pixel, and b is the background noise per pixel. From Eq. 1, it is clear that molecular localization may be significantly more precise than the optical resolution by a factor of as much as $\sqrt{N}$. Thus, the number of detected photons will be crucial to the enhancement of localization precision compared to resolution, as stated by condition 4. For a single molecule capable of emitting $\sim 10^5$ visible photons (e.g., emission wavelength $\sim$500 nm) before photobleaching, the position localization could be as precise as $\sim 500\ \text{nm}/(10^5)^{0.5}$ or a few nanometers. Considering the finite detection efficiency (typically $<5\%$) of modern single-molecule fluorescence microscopes, an estimate of the number of collected photons is $N_{\text{coll}} = \phi_{\text{det}}/\Phi_{\text{B}}$, where Φ_B is the photobleaching quantum yield for the molecule and ϕ_{det} is the detection efficiency, and the two-dimensional localization precision becomes

$$\sigma_{\text{x}}^2 = \frac{r_0^2 + q^2/12}{N_{\text{coll}}} + \frac{8\pi r_0^4 b^2}{q^2 N_{\text{coll}}^2} = \frac{\Phi_{\text{B}}(r_0^2 + q^2/12)}{\phi_{\text{det}}} + \frac{8\pi r_0^4 b^2 \Phi_{\text{B}}^2}{q^2 \phi_{\text{det}}^2}. \tag{2}$$

Since an increased b will increase σ_x^2, it is crucial that background be minimized, including background from inactive protein molecules (condition 5). Consider, now, N photoactivatable molecules subdivided into inactive (I), active (A), and bleached (B) states, with interconversion rates as follows:

$$\text{I} \underset{k_{\text{BC}}}{\overset{k_{\text{A}}\Phi_{\text{A}} + k_0}{\rightleftarrows}} \text{A} \xrightarrow{k_{\text{x}}\Phi_{\text{B}}} \text{B}, \tag{3}$$

where k_{A} is the activation excitation rate, Φ_A is the activation quantum yield, k_0 is the spontaneous activation rate, k_{BC} is the spontaneous and light-dependent inactivation rate, k_{x} is the fluorescence excitation rate, and Φ_{B} is the photobleaching quantum yield. These rate equations are similar to those shown to describe reversible photoconversion kinetics in related GFP mutants in the absence of photobleaching (30). Here, considering photobleaching and photoactivation, three linear coupled first-order differential equations then describe A, B, and I, the numbers of molecules in each state, respectively:

$$\frac{dI}{dt} = -I(k_{\text{A}}\Phi_{\text{A}} + k_0) + k_{\text{BC}}A \tag{4A}$$

$$\frac{dA}{dt} = -Ak_{\text{x}}\Phi_{\text{B}} + I(k_{\text{A}}\Phi_{\text{A}} + k_0) - k_{\text{BC}}A \tag{4B}$$

$$\frac{dB}{dt} = Ak_{\text{x}}\Phi_{\text{B}}. \tag{4C}$$

Alternatively, one of the three equations (4A–4C) could be replaced by the constraint that $A + B + I = \text{Const}$. Considering Eqs. (4A–4C), k_{A} and k_{x} can be chosen such that A, the number of active molecules within the illuminated region, is sufficiently sparse to allow simultaneous resolution and localization of those active molecules, and $\frac{dA}{dt} = 0$. The steady-state condition results in

$$A = I\left[\frac{k_{\text{A}}\Phi_{\text{A}} + k_0}{k_{\text{x}}\Phi_{\text{B}} + k_{\text{BC}}}\right] = \rho I, \tag{5}$$

where $\rho = \frac{k_{\text{A}}\Phi_{\text{A}} + k_0}{k_{\text{x}}\Phi_{\text{B}} + k_{\text{BC}}}$ describes a characteristic ratio of photoactivation to (reversible and irreversible) photobleaching that should span as wide a range of values as possible for maximum control over molecular readout. It should be pointed out that performing FPALM does not strictly require $dA/dt = 0$, since it will be possible to localize molecules as long as they are sparse enough to not have overlap in their point spread functions, but estimation of the conditions that yield an appropriate density of molecules (i.e., a certain favorable value for A) will be easier if $dA/dt \sim 0$ during the measurement. Typically, to control (limit) the number of active molecules at a given time (under irreversible photoactivation), the rate of photobleaching and spontaneous inactivation should be equal to or larger than the rate of activation, or $\rho \ll 1$. At saturation, where k_{x} is at or near maximum, the denominator of ρ will be maximum, and so ρ will be at its minimum (at a given activation rate), and that minimum ρ must be <1 (condition 2). Under this condition, if the number of inactive molecules I is approximately constant because $\frac{dA}{dt} \times t_{\text{m}} \ll I$(which should be satisfied anyway if $dA/dt = 0$), if $k_0 \ll k_{\text{A}}\Phi_{\text{A}}$, and $k_{\text{BC}} \ll k_{\text{B}}\Phi_{\text{B}}$ (condition 1), the ratio A/I can be adjusted over a wide range of values. The value of k_{BC} is expected to be very small for PA-GFP, since its activation process is irreversible (25,31).

Considering reversible photoactivation, it will be necessary under some condition for $k_{\text{BC}} \gg k_{\text{x}}\Phi_{\text{B}}$, so that the dominant path for limiting the number of activated molecules is by reversible deactivation rather than photobleaching. Also, to limit the number of active molecules, the deactivation plus photobleaching rate $k_{\text{BC}} + k_{\text{x}}\Phi_{\text{B}}$ needs to

be equal to or larger than the activation rate, which is again equivalent to $\rho \ll 1$, or condition 3.

We may estimate the desired value of A (the number of active molecules) by considering the area/molecule in comparison to the expected area of the molecule given by the $1/e^2$ radius of the point spread function (r_0) and the area covered by molecular (assuming nondirected) diffusion during the molecular readout time t_m:

$$\frac{S}{A} \gg r_0^2 + 4Dt_m, \tag{6}$$

where D is the diffusion coefficient, the FWHM of the PSF is $f_0 \sim \frac{0.55\lambda_m}{NA}$ (32), and $r_0 \sim f_0\sqrt{2\ln 2}$, λ_m is the emission wavelength, NA is objective numerical aperture, and S is the area of the illuminated region.

To ensure that Eq. 6 is satisfied by a constant dimensionless factor $\gamma \gg 1$, where γ is approximately the ratio of the area/molecule to the area of the PSF (e.g., $\gamma \sim 16$ for molecules to be separated by approximately an average distance of four times the size of their image on the relevant timescale), let the limit for straightforward simultaneous resolution and localization of particles require that

$$\frac{S}{A} = \gamma(r_0^2 + 4Dt_m) \tag{7}$$

or,

$$A = \frac{S}{\gamma(r_0^2 + 4Dt_m)}. \tag{8}$$

From Eqs. 5 and 8, it follows that

$$\rho I = \frac{S}{\gamma(r_0^2 + 4Dt_m)} \tag{9A}$$

and

$$\rho = \frac{S}{I\gamma(r_0^2 + 4Dt_m)}. \tag{9B}$$

Similarly, an estimate of χ, the maximum range of ρ, yields

$$\chi = \frac{\rho_{max}}{\rho_{min}} = \frac{k_A^{max}\Phi_A + k_0}{k_{BC}} \cdot \frac{k_x^{max}\Phi_B + k_{BC}}{k_0}, \tag{10}$$

which reflects the degree of control over the photoactivation readout and should be maximized experimentally. Thus, minimizing both k_{BC} and k_0 is essential for optimization of photoactivation readout. It also follows that in cases where $k_A^{max}\Phi_A \gg k_0$ and $k_x^{max}\Phi_B \gg k_{BC}$ (i.e., the spontaneous rates are small compared to the light-induced rates), maximization of the quantum yield for activation is helpful for control of the number of active molecules. Furthermore, a nonzero photobleaching quantum yield is also necessary, since otherwise the number of active molecules will become too large for resolution and localization. However, a large photobleaching yield will also reduce the total number of photons that can be detected per molecule and therefore reduce localization precision.

Estimation of imaging requirements for 80-nm and 20-nm localization precision

Using the theoretical model described above, the desired properties for a candidate PA-GFP and the parameters of the imaging system can be summarized. Consider now two cases: 1), imaging immobilized molecules at the demonstrated localization precision of 80 nm, and 2), imaging molecules mobile in two dimensions with $D \sim 0.08\ \mu m^2/s$ such as for influenza hemagglutinin (33) with a goal of ~20 nm precision.

Case 1. To have a representative sampling of molecules within a structure of size ~80 nm, one would roughly require ~100 molecules per 80 nm × 80 nm region within the image. For molecules uniformly distributed over a 10 μm × 10 μm area, this would require localization of 1.6×10^6 molecules. However, typical confocal images of cells contain highly heterogeneous distributions of molecules, and in many cases large regions of the image do not contain significant concentrations of fluorophore. Thus, estimating that a fraction of the image (e.g., 10%) contains labeled features of interest, the number of molecules needed N_{tot} is effectively lower ($N_{tot} \sim 1.6 \times 10^5$ molecules). Now, to estimate the acquisition timescale for such a number of immobile molecules, we employ the theory section derived previously in the text. Given that the image is ~10 μm × 10 μm, but ~10% of the image contains the majority of molecules, the area in which the molecules are effectively distributed is $\sim 0.1 \times 100\ \mu m^2 = 10\ \mu m^2$. To ensure that molecules are separated by 4 × r_0 on the average, we choose $\gamma = 16$ (Eqs. 7 and 8), which yields (from simulations) an ~9.7% chance of having two molecules within r_0 of each other. Using Eq. 8, $\gamma = 16$, and $r_0 = 0.281\ \mu m$, one estimates that $A \sim 8$ molecules/frame within the 10 μm^2 area should be activated. If one is willing to discard any molecules that are within r_0 of each other, the number of frames then is equal to $N_{tot}/A \sim 2 \times 10^4$ frames.

The next crucial factor determining time resolution is the imaging frame rate. The upper limit on frame rate is dictated by detected photon rate per molecule (η) and the photobleaching rate of molecules. The photobleaching rate should be optimized by using an excitation laser intensity where the photobleaching time is close to the image acquisition time (photobleaching times of $\ll$1 s are achieved routinely using high-intensity laser beams). The most obvious limitation in this case would be laser power at the readout wavelength. Second, the value of η at saturation for the fluorophore is crucial. Given a background noise estimated from measurements on coverslips to be $b \sim 1.02$ photons/frame/pixel (including readout noise), and pixel size $q = 0.121\ \mu m$, one can solve Eq. 2 to find that one needs $N_{coll} \sim 49$ detected photons/molecule to achieve

80 nm localization precision. For EGFP, $\eta_{EGFP} \sim 4 \times 10^4$ photons/s/molecule detected is typical at saturation in fluorescence correlation spectroscopy measurements (S. Hess, unpublished). Using the detected η for EGFP, it should be possible to detect 49 photons within a time of ~1.2 ms. Allowing for PA-GFP to have even a 10-fold lower saturating emission rate ($\eta_{PAGFP} \sim 4 \times 10^3$ photons/s/molecule including average brightness reduction due to flicker), 12 ms/frame should be enough to collect sufficient photons for the desired localization precision. Thus, the total acquisition time for 2×10^4 frames will be ~240 s. In the case of the sapphire sample, estimating a twofold higher background yields a $N_{coll} \sim 90$ photons, an acquisition frame time of 22.5 ms, and a total acquisition time of 450 s, which is the same order of magnitude as the actual acquisition time of 500 s. Note that this calculation assumes that the optimum (saturating) detected photon emission rate is achieved by the excitation (readout) laser. Thus, for a goal of 80 nm localization precision, the following parameters should be sufficient: $q = 0.121$ μm, $\eta > 4 \times 10^3$ photons/s·molecule, $b < 2$ photons/s·pixel, frame acquisition time of >20 ms, and a total number of detected photons before photobleaching of $N_{coll} = \phi_{det}/\Phi_B > 100$ (i.e., $\Phi_B < 2 \times 10^{-4}$ using $\phi_{det} \sim 2\%$). In practice, a number of parameters of the photoactivatable protein fluorophore, such as fluorescence quantum yield, extinction coefficient, fluorophore emission spectrum, flicker, and photobleaching properties, will affect the number of photons that are emitted. Detector quantum efficiency, objective numerical aperture, dichroic mirror and emission filters, and excitation laser intensity will also determine the number of emitted and detected photons.

Case 2. Now, to resolve features on ~20 nm length scales (i.e., $\sigma_x < 20$ nm) in samples with molecules randomly diffusing in two dimensions with $D = 0.08$ $\mu m^2/s$, N_{tot} increases to 2.5×10^6 for 10% coverage of a 100 μm^2 area at a density of 100 activated molecules within each area of 20 nm × 20 nm. Reading out the same number of molecules per frame (~8), the number of frames increases to $\sim 3 \times 10^5$ frames. Given a background level of 2.0 photons/s·pixel, the required number of detected photons per molecule increases to $N_{coll} \sim 440$, which will then require 110 ms/frame if the molecules are immobile, and an acquisition time of 3.3×10^4 s, or >9 h. If the molecules are mobile, an acquisition time of 0.2 s will be required because the molecular image will be spread by diffusion at $D \sim 0.08$ $\mu m^2/s$ such that $4Dt_m \sim 0.064$ μm^2 (from Eq. 6), which effectively blurs the image from a $1/e^2$ radius of $r_0 \sim 0.281$ μm to a larger radius $r_1 = \sqrt{r_0^2 + 4Dt_m} = 0.38$ μm, and requires an increase of N_{coll} to ~800 photons, yielding a total acquisition time of ~17 h. Thus, such measurements will require that the number of emitted photons before photobleaching (with detection efficiency $\phi_{det} \sim 2\%$) to be 4×10^4, which will require $\Phi_B < 2.5 \times 10^{-5}$, not a trivial constraint.

METHODS

Sample preparation

Samples of PA-GFP were prepared from stocks kindly provided by Dr. George Patterson (National Institute of Child Health and Human Development), by dilution 1:100, 1:400, or 1:1000 in high-purity water (HPLC grade, Sigma-Aldrich, St. Louis, MO) for a final concentration of ~400 nanomolar. A single one-microliter droplet of diluted PA-GFP solution was deposited on a No. 1.5 glass coverslip (Corning Life Sciences, Corning, NY) and allowed to slowly evaporate. The sample was then placed on the microscope stage and illuminated from below by the objective lens.

Illumination, photoactivation, and detection

Fig. 1 illustrates the principle of the method. Photoactivatable molecules (initially in an inactive, nonfluorescent state) are illuminated continuously by the ''readout light'', in this case an Ar+ ion laser. Next, the ''activation light'', a 405-nm diode laser, is turned on, which causes some of the inactive molecules (presumably a stochastically determined subset) to become active, but only a small enough number that they can all be resolved from one another. After those active molecules have been imaged for some time, they will spontaneously photobleach and become (permanently) nonfluorescent (or, in the case of reversibly photoactivatable molecules, they will be inactivated by the readout light). Images taken of the molecules as a function of time are then used to individually localize each fluorescent molecule and, after sufficient numbers have been analyzed, to construct an image at higher resolution than diffraction would ordinarily allow.

Fig. 1 *G* shows the key features of the experimental geometry. An Argon ion laser (10 W Innova 310, Coherent, Santa Clara, CA) was directed by steering mirrors through a dichroic mirror DM1 (435 EFLP EM XF12, Omega Optical, Brattleboro, VT) and into a focusing lens L1 ($f = 120$ mm) which was located in the rear port of an inverted microscope (IX71, Olympus America, Melville, NY) at one focal length from the back aperture of a 60 × 1.2 NA infinity-corrected water-immersion objective (UPLAPO60XW, Olympus). A second beam from a diode-pumped solid-state laser at 405 nm (BCL-405-15, low noise model, Crystalaser, Reno, NV) was directed onto DM1 to (upon reflection) be approximately colinear with the Argon ion laser beam. After passing through L1, both laser beams struck a second dichroic mirror DM2 (Z488RDC, Chroma Technology, Rockingham, VT) and reached a focus at the objective back aperture. Measured (unattenuated) power levels at the sample were 3.50 ± 0.04 mW of total Ar+ ion laser power (24.8% at 476.5 nm, 72.0% at 496.5 nm, and ~3.2% at <470 nm) and 0.197 ± 0.005 mW at 405 nm. Illumination by the 405-nm laser was controlled using a motorized filter wheel with RS232 interface and PC software (FW-102, Thorlabs, Newton, NJ), which was rotated into a completely transmitting (open) position for 10.0 ± 0.7 s, followed by return to a completely opaque position. The illumination intensity profile was approximately two-dimensional Gaussian with $1/e^2$ radii $r_0^{(405)} \sim 29.3 \pm 0.5$ μm and $r_0^{(Ar+)} = 41.6 \pm 0.5$ μm for the 405-nm and Ar+ lasers, respectively. Emitted fluorescence was collected by the same objective, filtered by DM2 and an emission filter (HQ535/50, Chroma).

Spectroscopy

Fluorescence was focused by the tube lens and reflected out the left side port into an optical fiber with 1-mm diameter, then detected by a PC-controlled spectrometer (USB2000FL, Ocean Optics, Dunedin, FL). Raw spectra were recorded every 100 ms unless otherwise noted, without boxcar or averaging, background-subtracted using a blank spectrum determined under the same conditions, then smoothed by boxcar with full width 4 nm.

Photoactivation microscopy

Fluorescence was focused by the tube lens and reflected out the right side port onto a CCD camera (Quantifire, Indigo Scientific, Baldock, Herts, UK)

interfaced by firewire to a PC. Images were collected by the CCD at 1.003 frames/s, gain of 11.4, and no binning (1 × 1) unless otherwise noted, then saved in raw (BMP or uncompressed TIF) format and analyzed using MATLAB scripts designed for particle recognition and localization. In brief, the algorithm searches for all pixels within the image above a threshold, assigning a single square region of interest (which in width is ~3 times the FWHM of the measured PSF) for each such pixel above the threshold, excluding all pixels within any other region of interest (ROI) closer than ~1.7 times the box half-width from any other ROI. The total number of pixels above a second threshold within each ROI is then determined. Those ROIs with at least 20 pixels above the second threshold are analyzed to determine the background-subtracted centroid. Only those pixels within the ROI that were above the second threshold are used to calculate the centroid. Because comparison of various algorithms for single-particle localization reveals that the centroid algorithm is susceptible to offset bias and degraded localization accuracy even at modest signal/noise ratios (S/N ~ 5) (28), the center of mass coordinates are then used as the initial guess for a least-squares Gaussian fit of the image of the fluorescent object (26):

$$I(x,y) = B + I_0 e^{-2[(x-x_0)^2 + (y-y_0)^2]/r_0^2}, \quad (11)$$

where B is the background pixel value, I_0 is the peak pixel value, x_0 and y_0 are estimated coordinates of the center of the fluorescent object, and r_0 is the $1/e^2$ radius of the point spread function. Although the PSF of a high numerical aperture lens is not strictly Gaussian (34,35), for distances less than the $1/e^2$ radius, a Gaussian is a reasonable approximation of the PSF, and is frequently used to fit the image of a point-like fluorescent object (16,26,27).

The overall magnification of the optical system results in a pixel size of 0.121 μm, which is within a factor of 2 of the standard deviation of the PSF (~0.20 μm) recommended for optimal localization precision in the presence of background (27). Analysis of mean pixel value as a function of the variance of the pixel value under the binning (1 × 1) and gain (11.4) settings used to obtain images yielded a slope of 11.7 ± 0.4 pixel values per photon and an intercept of −1.8 ± 3.3 (i.e., zero within uncertainty).

In practice, when the sample is first visualized, a number of molecules may already be activated by exposure to room light or spontaneous activation processes. The density of molecules may be higher than is optimal for localization of individual molecules, but as photobleaching progressively decreases the number of active molecules (in the absence of the activation laser), the density approaches a more manageable level and acquired frames can be analyzed to determine molecular positions. As the density drops below the desired value (e.g., 0.8 molecules/μm^2), the activation laser is pulsed at high intensity or turned on continuously at low intensity (such that the total dose per frame is between 4 and 40 J/cm^2). From that point on, frames are acquired until the majority of activatable molecules have been read out and photobleached. The density of molecules that are already activated at the beginning of the experiment (i.e., accidentally activated) depends largely on the age of the PA-GFP sample and whether it has been exposed to room light or left in buffer at room temperature for a significant time (i.e., days). Frozen protein stocks appear to last for approximately months without significant spontaneous activation (data not shown).

Simulations

For simulations, molecules were positioned randomly (100 at a time) within a 512 × 512-pixel region by generating a floating-point random number for both x and y coordinates of the molecule (not rounded off to the nearest integer). The image of the molecules was generated to include shot noise by stochastically distributing 1000 photons/molecule using a random number generator to determine whether a given pixel would receive a photon. The probability of detecting a photon at a given position was given by the point spread function (in this case a Gaussian centered at the x,y coordinates of the molecule, with $1/e^2$ radius of 1.6 pixels). Each pixel in the image then had a pixel value equal to the number of photons from the given distribution of molecules. Background of 10 ± 3 photons at each pixel was also added by a random number generator to the photons that form the image of the molecules.

Calibration sample

A 1 cm × 1 cm × 0.5-mm wafer of single-crystal sapphire (Princeton Scientific, Princeton, NJ) within 0.05° of R-cut was cleaned with acetone, isopropanol, then water, then annealed in air at 1700°C for 10 h, cooled to room temperature, then cleaned again by the same procedure. A 1-μL drop of PA-GFP (original stock diluted 1:100 in high-purity water) was then deposited on the surface and allowed to dry in air at room temperature in a darkened room. After drying, the sample was inverted and placed on top of a No. 1.5 coverslip (crystal surface with PA-GFP facing down) and was imaged from below by the objective. The sample was then imaged by FPALM as described above, using a Z496/10× laser cleanup filter (Chroma) to limit the excitation from the Ar+ ion laser to just the 496.5-nm line, yielding a power of 1.60 mW at the sample (496.5 nm line only), or an intensity of ~105 W/cm^2. Activation was achieved by an initial 2-s pulse of illumination at 405 nm with intensity ~40 W/cm^2 and by continuous illumination at 405 nm with ~4 W/cm^2 after the molecular density had reduced due to photobleaching (~500 s later); ~1000 frames were acquired at ~0.999 frames/s with an integration time of 0.983 s, gain of 11, and 2 × 2-pixel binning. The latter 500 frames were analyzed to determine the presented distribution of PA-GFP molecules.

Atomic force microscopy was performed using a JPSA (Manchester, NH) XE-100 microscope in contact mode on the same sapphire sample in various 1.5 μm × 1.5 μm areas of 256 × 256 pixels (not necessarily the same areas imaged by FPALM) with a stage with 50 μm travel, 1 line/s (256 s/image) rate, a new tip (radius <10 nm) with aluminum reflective coating (Budget Sensors, Sofia, Bulgaria), in air at room temperature.

RESULTS

Fluorescence photoactivation and emission under 405 nm and Ar+ ion laser illumination

Fig. 2 shows emission spectra from PA-GFP molecules dried on a glass coverslip and illuminated continuously by ~4.5 μW of power from the Ar+ ion laser and for brief (10-s) pulses of ~197 μW of 405 nm illumination. Negligible fluorescence was observed on coverslips without PA-GFP illuminated under the same conditions. During and after 405 nm illumination, the fluorescence emission within the detected wavelength range 510–565 nm significantly increased (Fig. 2, *C* and *D*). The observed emission maximum at 518 ± 2 nm (not corrected for detection or filter transmission efficiency), matches the expected emission of PA-GFP of 517 nm (25). The increase in fluorescence after 405 nm illumination indicates that a significant fraction of previously inactive PA-GFP molecules were activated. Under continuous Ar+ illumination in the absence of 405 nm activation, the PA-GFP fluorescence photobleached at a rate of 0.046 ± 0.002 s^{-1}. Successive activation attempts became less effective as a larger fraction of the original molecules had already been activated or photobleached. The fluorescence visible before application of the first 405-nm pulse (Fig. 2 *B*) indicates that a small fraction of the PA-GFP had already been activated.

Fluorescence microscopy of immobilized PA-GFP

Fig. 3 shows a typical time series of fluorescence images of a glass coverslip coated with a 1-μL drop of 1 nM PA-GFP,

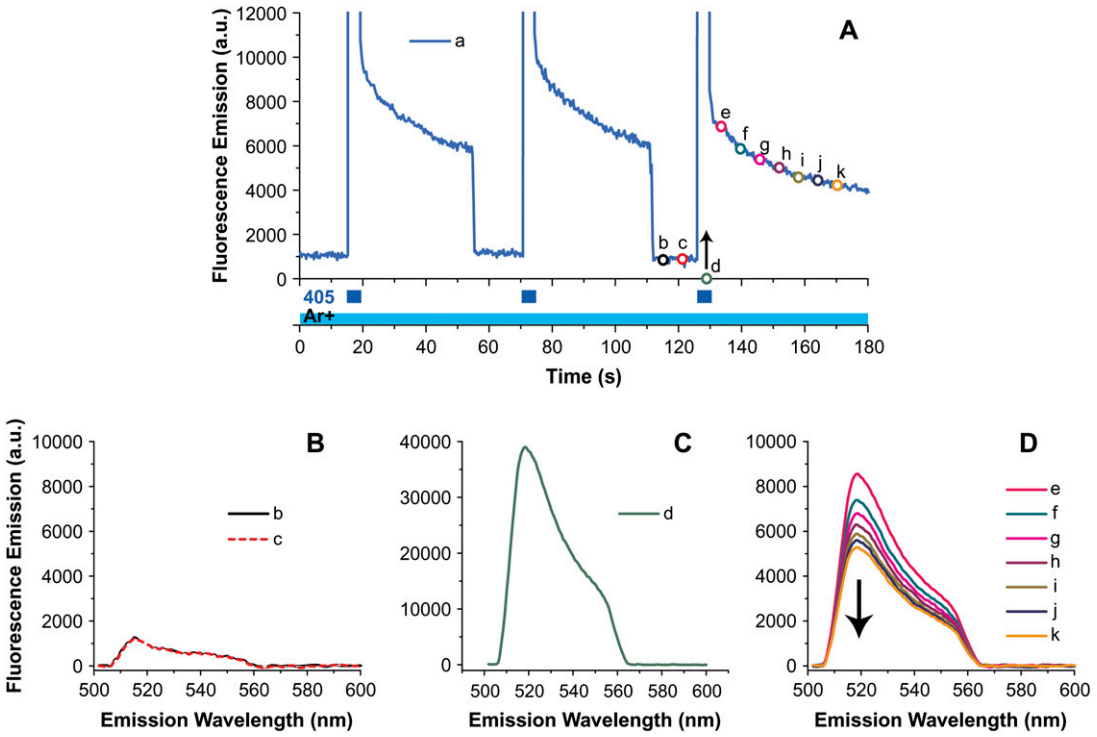

FIGURE 2 Fluorescence emission before and after photoactivation of PA-GFP. (*A*) Fluorescence emission spectra were measured as a function of time as PA-GFP molecules immobilized on a glass coverslip were illuminated continuously with an Ar+ ion laser (time dependence shown by *long, light blue bar* along time axis), and intermittently with a 405-nm laser (*short, dark blue bars* just above the axis). The background-subtracted integrated area under the fluorescence spectrum is plotted as a function of time (*blue curve a*). Downward red arrows indicate movement of the sample to a new area that had not been illuminated previously. Under continuous illumination at 488 nm, the fluorescence intensity increased significantly during illumination with the 405-nm laser. The emission spectra at various times before activation (*b* and *c*), during (*d*), and after (*e–k*) correspond to curves shown in *B–D*. The downward black arrow in *D* indicates that the emission intensity was decreasing with time.

activated previously by 10 s of illumination at 405 nm at an intensity of 7.3 W/cm^2 (~197 μW at the sample). The sample was excited continuously by 64 W/cm^2 of Argon ion laser illumination (3.5 mW at the sample, including both the 476.5-nm and 497.5-nm lines) and imaged by CCD using ~1-s exposures (Fig. 3 *A*). The discrete on-off behavior of various spots as a function of time (Fig. 3, *B–F*), and their FWHM of typically 0.30 ± 0.06 μm, which is consistent with the expected FWHM of 0.55 λ_m/NA ~ 0.237 μm (32) at the maximum emission wavelength $\lambda_m = 517$ nm, indicates that the observed spots are single fluorescent molecules.

Localization of single molecules

Simulation results

Fig. 4 *A* shows results from the algorithm for identification and localization of bright spots in fluorescence images of PA-GFP molecules. Briefly, pixels within the image with intensity above a threshold (pixel value 30) are identified and marked with an ROI of 7 × 7 pixels (0.85 × 0.85 μm^2). Any ROI which was <0.73 μm (6/7 times the full width of the box) from any other ROI was excluded (distance measured center to center). ROIs are further selected for those with at least 20 pixels above a second threshold (pixel value 3) after background subtraction. Selected boxes are analyzed for centroid (Fig. 4 *A*, *blue lines*) and the centroid coordinates are then used as an initial guess for an unweighted Gaussian least-squares fit of the intensity within the box using Eq. 11 and a fixed $r_0 = 1.6$ pixels = 193 nm.

Fig. 4 *B* compares the precision of the localization routine using simulated images and either a 1), centroid-after-threshold-and-background-subtraction algorithm, or 2), Gaussian-fit-after-threshold-and-background-subtraction algorithm with initial position guess given by the centroid. The histograms of position deviation are shown for 19,706 total simulated molecules arranged randomly in a 512 × 512 image with 1000 photons each and PSF $1/e^2$ width of 1.6 pixels. The distribution of deviations for the centroid show significantly (>20-fold) larger systematic offset 0.0273 ± 0.004 pixels compared to 0.00116 ± 0.00012 pixels for the same objects localized by Gaussian fit. The $1/e^2$ width of the distribution of deviations (0.088 pixels for centroid and 0.105 pixels for Gaussian fit) was similar, consistent with the high signal/noise ratio of the simulated particle images. The values are slightly higher than the expected $1/e^2$ width of $2/\sqrt{N} = 0.063$ pixels in the ideal case without background and indicate that the algorithms can certainly be improved, but also reflect additional sources of noise such as pixelization.

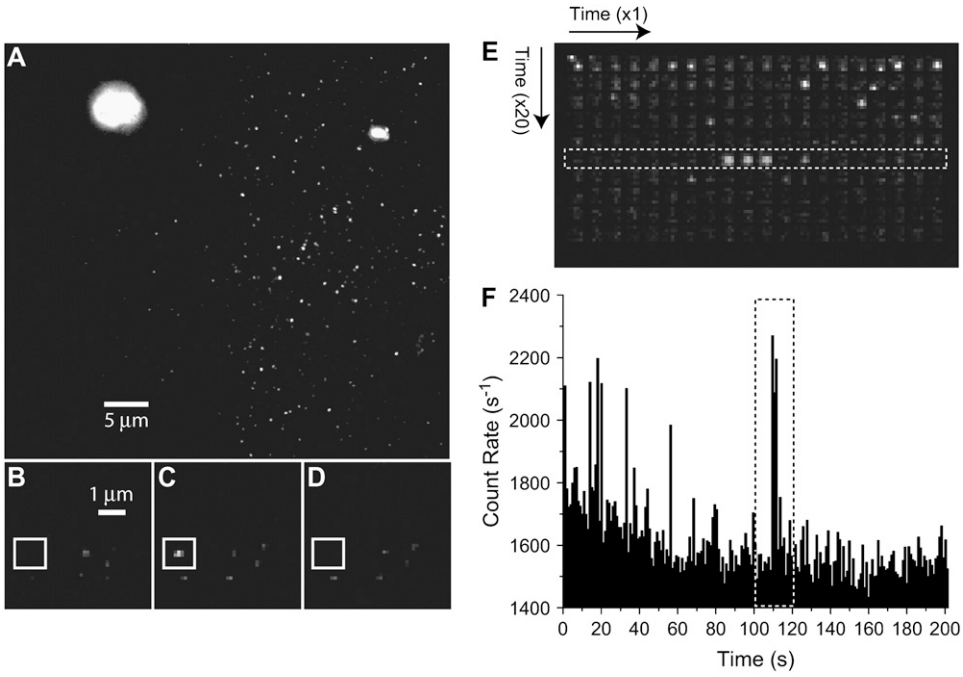

FIGURE 3 Imaging single molecules of PA-GFP. (*A*) Single frame (1-s acquisition) from a time series of images of PA-GFP molecules at low density on a glass coverslip illuminated continuously by an Ar+ ion laser and activated by brief pulses from a 405-nm diode laser. Fluorescence was detected from 510–560 nm. (*B–D*) Three successive 1-s frames in the same series showing discrete on-off behavior expected for a single fluorophore. All images had the same constant offset subtracted and all pixels were multiplied by a second common constant for display purposes. (*E*) Collage of images from a longer time series of a 5 × 5-pixel region (~0.6 μm × 0.6 μm) imaged at 0.998 frames/s for 200 s (images are arranged from left to right, in rows of ~20 s each). (*F*) Count rate within the 5 × 5 region as a function of time shows discrete behavior. The dashed box in *F* highlights the time dependence of the count rate in the series of images in the white dashed box in *E*.

Fig. 5 shows the results of a simulated distribution of molecules placed along periodic vertical strips 60.5 nm wide separated by regions 60.5 nm wide without molecules. Although such a structure would be difficult to resolve using standard light microscopy, the periodicity is visible in the plot of localized molecular positions.

Experimental results

An FPALM image of a drop of PA-GFP dried on a coverslip, obtained after brief 405-nm illumination and acquired under continuous Argon ion laser illumination is shown in Fig. 6. After an initial period of intense fluorescence emission from a relatively large number of activated molecules, photobleaching reduced the number of fluorescent molecules to yield a low enough density for resolution and localization of between 50 and 200 molecules per acquired (~1-s) frame. Fig. 6 *A* shows the tabulated and plotted positions of 48,746 PA-GFP molecules localized during a continuous illumination and image acquisition of 399 s (400 frames). Presentation of these positions at successively higher zoom is shown in Fig. 6, *B–D*. Fig. 7, *A–C*, presents the molecular positions as dark circles on a light background and zooms in on a different region. Fig. 7 *D* overlays the position of each localized molecule with a circle equal in radius to r_0, the calculated $1/e^2$ radius of the point spread function for the 1.2-NA objective and a 520-nm emission wavelength. Note that many of the spots due to single molecules are closer together than r_0 and would be difficult to resolve if they were emitting simultaneously. Note also the nonuniform distribution of molecules on the coverslip surface, which presumably results from the evaporation pattern of the water droplet containing

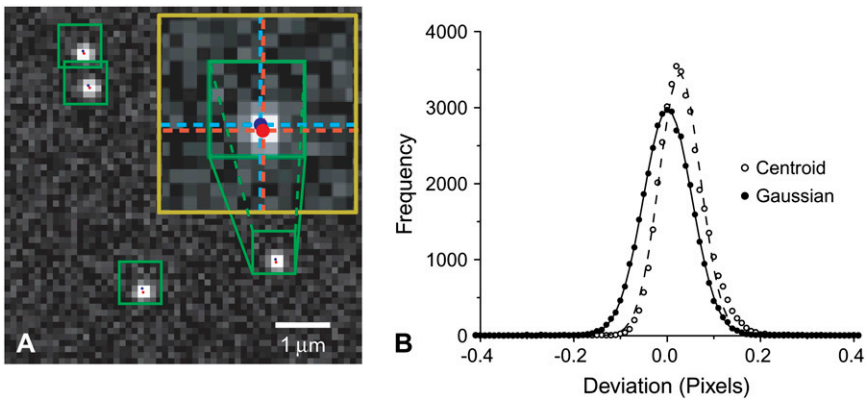

FIGURE 4 Single particle localization algorithm. Simulated images containing single particles were analyzed to compare the accuracy and precision of the centroid algorithm and Gaussian least-squares fit methods for particle localization. The simulated image (*A*) was processed to find pixels above a threshold and assign a nonoverlapping ROI for each one (minimum center-to-center ROI separation was 0.86 times the box full width). Centroid analysis was performed on ROIs with >20 pixels above a second threshold, and those coordinates (inset, *dashed blue lines*) were used as an initial guess for a Gaussian least-squares fit with the image using Eq. 11 (coordinates from the Gaussian best fit are shown in *red*). (*B*) Tabulation of the localization error for randomly positioned simulated molecules shows that the centroid algorithm has similar precision (curves shown are fits to a Gaussian distribution) but has a systematic bias. The Gaussian algorithm has less systematic bias and similar or better precision (particularly at low signal/noise ratio) (28) and was therefore used for subsequent analysis of the experimental images.

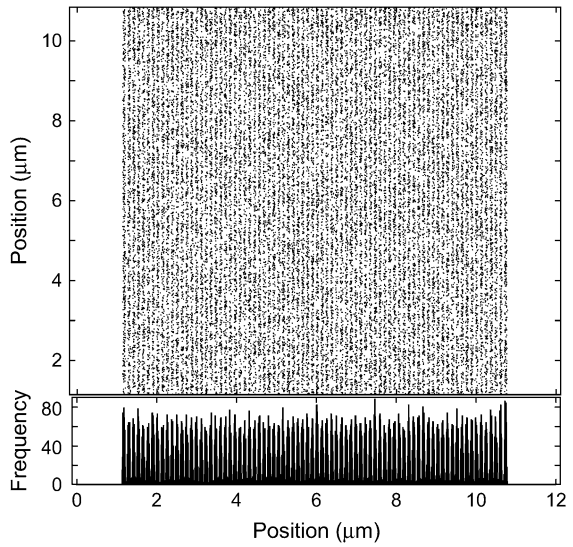

FIGURE 5 Simulated FPALM resolves a subdiffraction-scale structure. Simulated photoactivatable fluorescent molecules were distributed in periodic narrow vertical strips 60.5 nm wide, separated by 60.5-nm gaps. The molecules were activated stochastically in small numbers (~50) per frame and simulated to emit photons, 1000 of which were detected. The simulated PSF was 200 nm wide (FWHM). Molecules were localized by the Gaussian algorithm described in Methods and in Fig. 4. A plot of 30,659 molecular positions determined by the algorithm demonstrates the ability of the technique to resolve structures smaller than the PSF. The histogram of particles observed within horizontally-spaced bins, each spanning a 10 nm range in x-coordinates only (shown directly below the plotted position), also reveals the subdiffraction periodicity of the simulated sample.

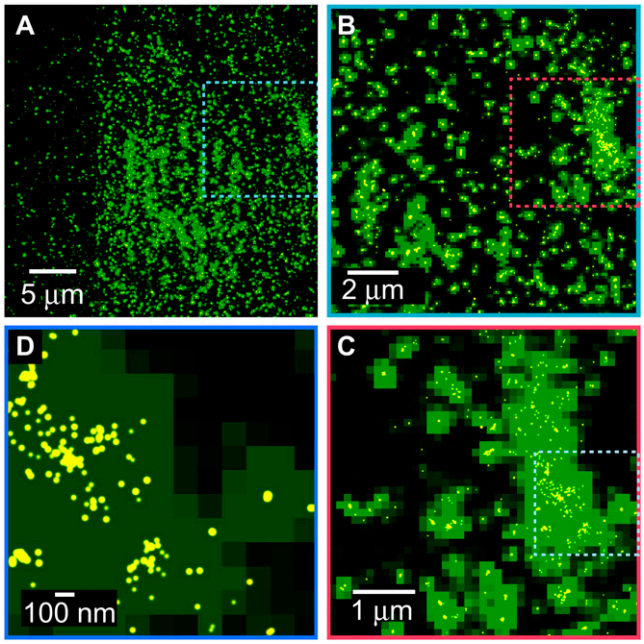

FIGURE 6 Measured FPALM images of PA-GFP on a glass coverslip. (*A–D*) Measured positions of 48,746 localized molecules are plotted in yellow, weighted by the peak intensity at the center of the molecule, obtained from a Gaussian fit of the image using Eq. 11. The molecular positions from FPALM are plotted on top of the sum of all the widefield fluorescence images obtained during the acquisition (sum image shown in *green*) to illustrate the significantly greater resolution of FPALM compared to widefield fluorescence microscopy. The sequence from *A* to *D* progresses toward higher zoom, where the dotted box shows the region being expanded (e.g., the dotted red box in *B* shows the same region as all of *C*). In *C* and *D*, heterogeneity on length scales shorter than the classical diffraction limit is clearly visible.

the PA-GFP. Features and structures much smaller than the diffraction-limited resolution ($r_0 \sim 0.61\ \lambda/\mathrm{NA} = 264$ nm) are clearly visible, especially in the higher zoom panels. Molecular positions in Fig. 6 are plotted on top of the sum of all widefield images obtained during the acquisition. The summed image is essentially equivalent to the widefield image of the same measured distribution of molecules if they had all been fluorescent simultaneously, and were imaged using the same laser illumination profile. As expected, much of the structure observed by fluorescence photoactivation localization microscopy is lost when the images are summed.

Fig. 8 shows a plot of measured molecular positions of PA-GFP dried on an annealed sapphire crystal surface that contained terraces spaced by 200–630 nm, as imaged by atomic force microscopy (AFM). The terraces in most cases consisted of a vertical step of ~0.33 nm, which is close to the expected step thickness for single atomic monolayers in sapphire in this crystal orientation, followed by a gradual linear decline in height, which when repeated over many micrometers resembles a sawtooth pattern. The PA-GFP was observed to often localize along periodic arrays of parallel lines, which can be seen in Fig. 8 *A*. Note also the asymmetry of the distribution on either side of the ridges, which demonstrates a higher molecular density approaching the ridge from one side and a lower density on the other side of the ridge. The scale of the AFM image inset is the same scale as the plotted molecular positions. Analysis of the distribution of molecular positions along the direction perpendicular to the ridges (Fig. 8 *B*) reveals the width of the step, as resolved by FPALM, to have a FWHM of 86 ± 4 nm, which is significantly less than the FWHM of ~238 nm that would be observed by widefield microscopy with the same numerical aperture (NA = 1.2) and emission wavelength ($\lambda_m \sim$ 520 nm).

PA-GFP molecules were observed to activate slowly (with an ~5- to 10-s timescale) under continuous unattenuated Ar+ laser illumination, in the absence of 405 nm illumination. The wavelength intensity spectrum of the Ar+ laser measured at the sample was found to contain a small fraction (<3%) of its intensity at $\lambda < 470$ nm, which presumably causes activation in the absence of 405 nm illumination. Activation was not observed in the absence of 405 nm light when a cleanup filter (Z496/10×) was included in the Ar+ laser path that passed only the 496.5 nm line. A portion of the PA-GFP was found to be activated before we illuminated it with the 405-nm laser (data not shown), which contributed to the initially large number of molecules in the field of view.

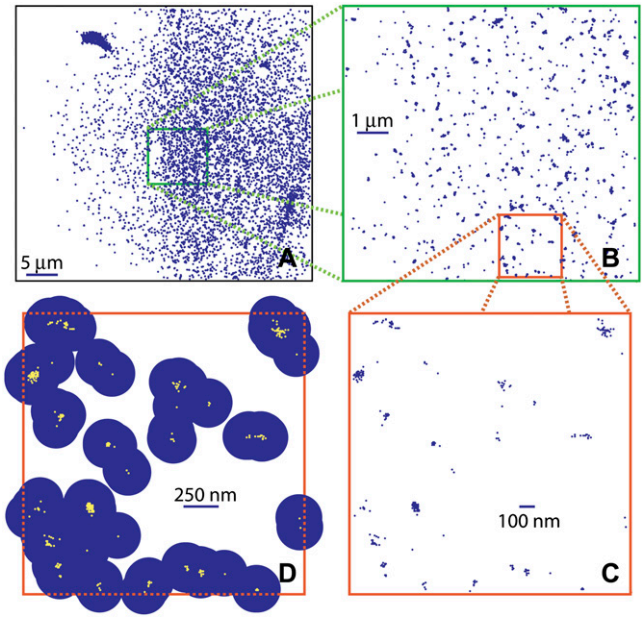

FIGURE 7 Second representation of measured molecular positions obtained by FPALM. (*A–C*) Blue dots indicate the location of a single PA-GFP molecule, determined by FPALM, of the same acquisition series shown in Fig. 6. (*D*) After zooming in >30-fold from *A* to *C*, the positions are replotted as yellow dots surrounded by a blue disk, approximating the lateral extent of the observation PSF, to emphasize the difficulty one would have in resolving these molecules simultaneously by standard widefield microscopy.

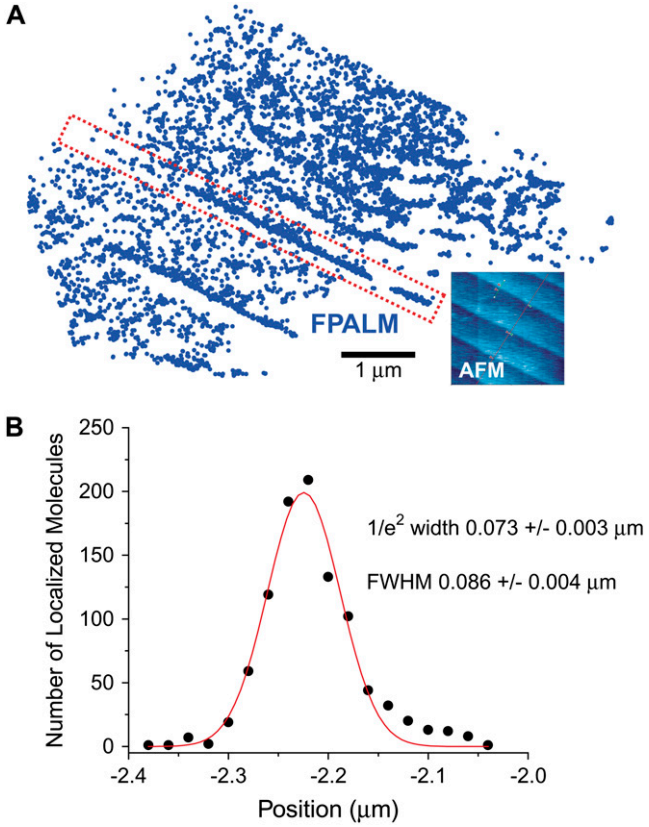

FIGURE 8 FPALM image of an R-cut single-crystal wafer of sapphire annealed at high temperature to produce atomic terraces, labeled with PA-GFP. (*A*) The positions of PA-GFP molecules localized over a period of 500 s are plotted (*blue points*) and compared with an atomic force microscope (AFM) image (*inset*) of the same sample (not necessarily the same area). Atomic step dislocations spaced laterally by 200–630 nm are visible by both techniques, because the PA-GFP has localized to those dislocations upon drying. Scale bar (1 μm) applies to both the FPALM and the AFM images. Note the gradient in particle density across the dislocations shown by FPALM. The red dotted box corresponds to the profile in *B*. (*B*) Analysis of the profile of a dislocation. The histogram of molecular positions (*black points*) as a function of distance perpendicular to the dislocation reveals the width of the feature as visualized by FPALM. Fitting the profile with a Gaussian (*red line*) yielded a $1/e^2$ half-width of 73 ± 3 nm, and an FWHM of 86 ± 4 nm.

In addition to high-resolution imaging of the molecular distribution, FPALM can be used to quantify other single-molecule properties of the fluorophores, which are inaccessible to standard widefield fluorescence microscopy. Fig. 9 shows the brightness distribution of localized molecules and the time dependence of the number of localized molecules. Under continuous Ar+ illumination, the number of fluorescent particles decayed as a single exponential with a $1/e$ time of 125 ± 3 s.

DISCUSSION

FPALM is capable of imaging entire cells or multiple cells, with localization precision of the order of tens of nanometers, and potential for even better precision. The experimental setup consists of a fluorescence microscope, a CCD camera, and two commercially available CW lasers. Images can be acquired with modest alignment and setup time. Single molecules are localized individually, allowing their position and brightness to be measured and analyzed to extract spatial and kinetic information that is inaccessible when large numbers of molecules are observed simultaneously. Unlike other single molecule imaging methods, the maximum labeling density suitable for localization can be orders of magnitude larger than the ~1 fluor/μm^2 (for each nonoverlapping spectroscopic channel) dictated by the optical Rayleigh criterion. This allows for a much more complete picture of the spatial distribution of the species of interest, while still providing single-molecule sensitivity. In principle, position analysis of a given molecule as a function of time can be achieved to estimate the velocity. FPALM does not require scanning either the beam or the sample, as is necessary in RESOLFT (including STED), 4Pi, and standard confocal microscopy (6,13,15). Furthermore, the sample is illuminated by a relatively low intensity (<100 W/cm^2) compared to that used in confocal microscopy (i.e., ~10^4 to 10^5 W/cm^2), reducing the deleterious affects of unwanted photobleaching and cell damage.

FPALM has been demonstrated as a means of imaging structures on subdiffraction length scales, which has been confirmed by atomic force microscopy. The distribution of

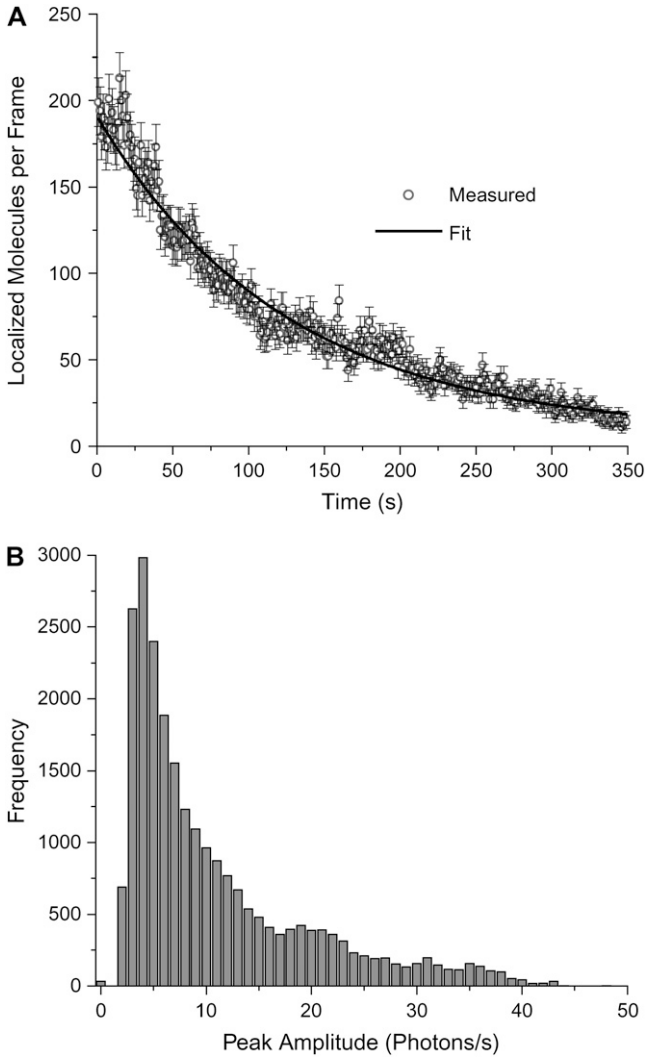

FIGURE 9 Additional information, not available to ensemble fluorescence microscopy methods that image large numbers of molecules ($\gg$100) simultaneously, is obtained by FPALM. (*A*) The number of molecules fluctuates and decays with time as FPALM frames are acquired. The number of fluorescent molecules within the observation volume in a widefield or confocal fluorescence microscope is difficult to determine without a calibration standard, but is obtained for every image in FPALM. A single exponential time constant ($\tau = 125 \pm 3$ s) described the decay of the number of molecules observed, consistent with depletion of a single reservoir of inactivated PA-GFP molecules. (*B*) The distribution of single-molecule fluorescence intensities is determined by FPALM and converted into the detected photon count rate at the center of the diffraction-limited image of the molecule. All amplitudes had a constant subtracted to account for background. Such information is useful in determining the degree of heterogeneity within a population of molecules and is typically difficult to obtain from measurements that sample large numbers of molecules simultaneously.

molecular positions at the edge of a terrace shows a $1/e^2$ width of $\sim$73 $\pm$ 3 nm, or a FWHM of 86 $\pm$ 4 nm, which is significantly less than the diffraction limit in normal widefield microscopy. AFM imaging revealed that the sharp side of the vertical steps from terrace to terrace occurred over a lateral distance of 79 $\pm$ 9 nm, in good agreement with the value determined by FPALM. Although the above FWHM shows that subdiffraction features can be resolved, the FWHM is also degraded by background from the sapphire, which was higher than in the samples of PA-GFP on coverslips, and therefore the ultimate resolution of FPALM may be much better than has been shown here. Nonetheless, the profile of the features and their spacing as determined by FPALM are consistent with AFM results, confirming that the method can be used to visualize structures on length scales shorter than the diffraction limit.

The time dependence of the fluorescence emission of single fluorophores can complicate localization analysis (26). Due to the relatively long ($\sim$1-s) integration times in the FPALM results presented here, the flicker and blinking that occur on the microsecond and millisecond timescales is averaged over, and therefore not directly observed. However, some blinking on longer timescales (Fig. 3) is still observed. In addition, long integration times will allow for significant movement to occur if the molecules are mobile. When random molecular diffusion occurs on timescales shorter than the integration time per frame (here $\sim$1 s), the image of the molecule will be blurred, with fewer detected photons per pixel distributed over a larger number of pixels. Molecules moving in three dimensions during the acquisition time will be extremely difficult to localize by the current implementation of FPALM. On the other hand, consider molecules constrained to move in two dimensions (i.e., within the focal plane of the microscope). In this case, under random diffusion, the mean position of each molecule is expected to remain unchanged, whereas the variance is expected to increase according to $r_0^2 + 4Dt_m$, where r_0 is the $1/e^2$ radius of the diffraction-limited PSF (see also Eqs. 6–8). Because of the larger variance and reduced signal/noise and signal/background ratios per pixel, the ability to determine the mean position will be significantly diminished. In the special case of random two-dimensional motion with a very small diffusion coefficient ($D < 10^{-10}$ cm^2/s), localization may in principle still be possible.

If significant nonrandom motion occurs during the acquisition time, the image of a given molecule will no longer appear circular, also making analysis much more difficult; new methods of analysis will likely need to be developed. Although this complicates the determination of the mean position within a single image, successive images can be analyzed to determine molecular velocities (as is done in FSM), which is certainly of biological relevance (21–24). FPALM is particularly well-suited to the study of proteins and other structures in fixed cells, and is possibly applicable to a subset of membrane proteins in living cells, if their lateral mobilities are at least two orders of magnitude smaller (33) than those of soluble (i.e., cytosolic) GFP-tagged proteins (36–38). Successful examples of single-molecule total internal reflection fluorescence (TIRF) detection with high signal/noise ratio in agarose (39) and membranes (40) offer a promising complement to single-particle tracking

measurements that have revealed time-dependent lateral heterogeneities in biological membranes (41,42).

The power offered by genetic manipulation of fluorescent proteins (43–46) is a significant advantage for FPALM, since any protein of interest can be labeled by splicing the gene for that protein into a PA-GFP or other photoactivatable fluorescent protein (PAFP) construct. Multiple labeling is possible using combinations of photoactivatable proteins with different activation and emission spectra. Labeling of other cellular species, such as lipids, will rely on development of conjugates with photoactivatable organic dyes, PAFP-tagged antibodies, or lipid binding proteins such as the pleckstrin homology domain that binds PIP_2 (47). As the variety of available PAFPs increases (31), multi-color labeling experiments using FPALM will become even more flexible. Mutagenesis of existing PAFPs can also be used to reduce blinking and undesirable types of spectral switching that complicate the use of many types of fluorophores, such as quantum dots, in single-molecule imaging. The quantum yield of PA-GFP (0.79) is already quite high in comparison to most other PAFPs (25,31). Comparison of fluorescence intermittency of PA-GFP mutants by fluorescence correlation spectroscopy has shown significant variation in the degree to which these proteins flicker, which can limit the number of photons emitted per second per molecule (S. Hess and G. Patterson, unpublished results). Improvement of the photophysical properties of PAFPs to reduce intermittency and increase photon emission rate will allow even greater localization precision to be achieved.

The irreversible photobleaching that fluorophores inevitably undergo is advantageous in FPALM since it helps control the number of fluorescent molecules in the field of view during each image frame (time point). Although it is expected that photobleaching will lead to the production of chemically reactive species that could be toxic to living cells, the number of bleached molecules produced is of the same order of magnitude as those produced in confocal microscopy experiments (it is not uncommon for a significant portion of the fluorophore to be bleached during the acquisition of a z-stack with frame averaging, for example).

The time required by a fluorophore to be photoactivated (the ''settling time'' mentioned by Hoffman et al.) can also limit imaging rate in scanning photoactivation microscopy (15) but is not as significant an impediment in FPALM because the entire field is imaged at once, and each frame is acquired over a timescale of seconds or fractions of a second, rather than the typical microsecond voxel dwell time in confocal and other scanning microscopies. Also, under some conditions in other types of photoactivation microscopy, it becomes difficult to increase the activation rate past a certain point (15). In comparison, activation rates for PA-GFP much larger than the frame rate ($>10\ s^{-1}$) have been achieved with modest activation laser intensities ($\sim$100 W/cm^2, data not shown) and since it is not anticipated that the frame rate would need to exceed $\sim 10^2\ s^{-1}$, the same kind of limitation for FPALM using PA-GFP may not exist. Further study of the activation rate as a function of activation laser intensity is needed, since the activation rate and photobleaching rate can limit the acquisition frame rate.

Although many fluorescent proteins are known to spontaneously aggregate, point mutations such as L221K can be introduced into PA-GFP (which is of the family of green fluorescent proteins and is less susceptible to aggregation, with $K_d \sim 0.11$ mM) to raise (improve) the K_d to $\sim$9 mM (48).

Recent work in single-molecule fluorescence microscopy has focused on improving the ability to resolve multiple fluorophores by spectral separation (16); nanoparticles such as quantum dots offer somewhat narrower emission spectra and therefore can be ''packed'' in larger numbers into the same range of visible wavelengths (49). However, in comparison to fluorescent proteins, quantum dots have so far proven to be more difficult to target to some intracellular compartments, especially the nucleus (50). FPALM obviates the need for multiple detection channels by controlling the number of particles that are fluorescent at a given time, such that even at high inactive probe concentrations, the distance between active (fluorescent) molecules is on the average much larger than the resolution. It should be noted that extending this technique to multiple spectral channels is possible, and would result in a modest increase in the possible labeling density, proportional to the number of spectral channels, but a much more significant advantage of labeling with multiple, spectrally distinct photoactivatable species is simply to be able to visualize multiple species at high resolution.

Estimated signal/noise ratio

We use the definition of signal/noise ratio $S/N = (I_0 - I_B)/\delta$, where δ is a representative noise level and $I_0 - I_B$ is the difference in mean intensity between the object and the background (Cheezum et al.), to obtain for the molecule in Fig. 3 E: $I_0 - I_B \sim 161$ photons and $\delta \sim 25.6$ photons, for $S/N \sim 6.3$, which is high enough to allow localization with distance precision $>$100 nm using a Gaussian algorithm, but not necessarily with other algorithms (Cheezum et al.). The expected excitation rate $k_x = \sigma I$, where σ is the one-photon excitation cross section and I is the excitation intensity in photons/unit area/s, can be estimated theoretically considering the excitation laser (Ar+) power (6.7 mW) in the back aperture, the objective transmission coefficient ($\sim$0.5) for the appropriate wavelengths (476.5 nm and 496.5 nm), the $1/e^2$ radius of the illuminated area (41.6 $\pm$ 0.5 μm), the resulting intensity $\sim$46 W/cm^2 at 496.7 nm and $\sim$16 W/cm^2 at 476.5 nm, the energy per photon, and the estimated extinction coefficient at 476.5 nm and 496.7 nm (using $\varepsilon =$ 17,400 $M^{-1}\ cm^{-1}$ at 504 nm and wavelength dependence from Patterson et al. (25)), to obtain excitation rates $k_x^{(497)} \sim 6.2 \times 10^3\ s^{-1}$ and $k_x^{(477)} \sim 1.3 \times 10^3\ s^{-1}$. The expected detected photon count rate per molecule (η) is estimated by

$\eta = \varphi_{fl}\left(k_x^{(497)} + k_x^{(477)}\right)\phi_{det}$, where $\phi_{fl} = 0.79$ is the fluorescence quantum yield, and ϕ_{det} is the overall detection efficiency, estimated as 2%, to yield the ~120 photons/s expected, which compares fairly well with the average (measured) collected photon rate of ~40–180 s^{-1} estimated from the histogram of detected molecular count rates (Fig. 9 *B*) and the FWHM of the PSF. The average time before photobleaching, $\tau_B \sim (k_x\Phi_B)^{-1}$, is calculated using estimated photobleaching quantum yield, $\Phi_B \sim 5 \times 10^{-5}$, slightly higher than for EGFP (25) to obtain $\tau_B \sim 2.7$ s, which is consistent with our observation of PA-GFP molecules for a few frames before photobleaching. For simplicity we use the same photobleaching yield at both 477 nm and 497 nm, although experimental results do show some dependence of Φ_B on excitation wavelength in EGFP (51).

Constraints on activation and deactivation rate constants

Given that we need to activate molecules at a rate of $\sim 0.8/\mu m^2$ per frame (for sufficient spatial separation), using Eq. 4B, the number of activated molecules/μm^2/s in the imaging area *S* will be $\frac{1}{S}\frac{dA}{dt}$, which should roughly equal $0.8/\mu m^2$ times the frame acquisition rate. For example, for a 50-Hz frame rate, one would need $\frac{1}{S}\frac{dA}{dt} \sim 40/\mu m^2$ s. Since observed activation times of less than a few milliseconds in PA-GFP have been reported in a confocal geometry (25), it will usually be possible to meet the desired rate by adjusting the excitation laser power. In contrast, ensuring that the rate of activation is low enough is more difficult due to the possibility of a spontaneous activation rate (k_0) and readout-beam-induced activation, which could become particularly significant when a large reservoir of inactive molecules is present. The product of $k_0 \times I/S \ll 0.8/\mu m^2$ will ensure that most activated molecules are separated by more than the diffraction-limited radius of the PSF. As the inactive reservoir is depleted, the activation laser intensity could be increased to keep the number of activated molecules per frame constant (8 in this case), which will minimize delay in readout of a sufficient number of molecules. Although the spontaneous deactivation rate is expected to be very low in PA-GFP due to irreversible decarboxylation of the chromophore during photoactivation (25), further study of deactivation rates in photoactivatable proteins using single-molecule methods and fluorescence correlation spectroscopy would likely be useful.

Comparison to other high-resolution fluorescence methods

Methods such as nanometer localized multiple single-molecule fluorescence microscopy can resolve and localize multiple (>5) molecules within close proximity, but the precision of localization will degrade as larger numbers of molecules fall within the same diffraction-limited spot. FPALM is able to localize in principle a very large number of molecules within a diffraction-limited region as long as they are activated and localized in small numbers at a time. For example, PA-GFP molecules were localized (within one region) at a density of 83 spots within a 0.1 μm × 0.12 μm area (Fig. 6), or ~6900/μm^2. The acquisition rate so far (~50,000 molecules localized in ~400 s) is slow compared to confocal microscopy, but comparable to other ''super-resolution'' techniques such as 4Pi and nanometer localized multiple single-molecule (6,16).

In principle, the localization precision can be significantly improved. Demonstrated precisions in the range of 2 nm have been realized (52,53). One of the current limitations with this work (using PA-GFP) is the number of detected photons before photobleaching, and the background generated by fluorescence of the inactive form of the protein (among many sources).

Because of the low excitation intensities used in FPALM compared to STED, there is no need to engineer complex optics to align a stimulated emission beam intensity null with the center of the focus of another beam. Power levels similar to those described in ''low-power'' RESOLFT-type microscopies can be used.

A short photoactivation time (less than the pixel dwell time) is important in scanning RESOLFT-type microscopies (15) whenever photoactivation or other relevant photophysics must occur during the pixel dwell time. Although the photoactivation time can be long (>1 s) in FPALM, since it is not a scanning method, rapid molecular readout followed by rapid inactivation or photobleaching is important because it limits the temporal resolution of the method, which can influence spatial resolution. For example, if molecules are moving nonrandomly, then the localization algorithm will have trouble determining the center of the image of the molecule and therefore the precision of position determination will be reduced. However, if the molecules are diffusing randomly in two dimensions, they can still be localized with the same algorithm and their positions determined with precision higher than the diffraction-limited resolution. A further constraint to such a procedure is that the mean-squared distance between fluorescent (active) molecules still must exceed (by a large factor) the resolution-squared plus the mean-squared displacement due to diffusion during the acquisition time per molecule (i.e., the time per frame).

Activation and readout by a single (Ar+) laser beam is advantageous because it obviates the need for alignment of multiple excitation sources (simplifying alignment), but it also reduces the degree of control over relative intensities of the activation and readout illumination, and therefore reduces the degree of control over the number of active molecules visible at a given time. The inactive form of PA-GFP absorbs from <350 nm to ~450 nm (54), and activation at 435 nm by one photon has been observed (54), suggesting that activation is possible using wavelengths other than 405 or 413 nm.

These results and the rapidly developing field of nonlinear subdiffraction microscopies point to a need for fluorescent probes with nonlinear properties (i.e., strong STED or strong photoconversion). The conditions for effective FPALM also

reveal a need for minimal spontaneous photoconversion rates in PA-FPs, as well as for RESOLFT microscopies that use PA-FPs (15).

FPALM is much more straightforward for two-dimensional imaging of molecular distributions, where the molecules of interest are all located between two planes separated by $d \ll z_0$, and z_0 is the depth of field (axial extent of the point spread function). FPALM does not come close to the time resolution offered by three-dimensional single-particle tracking (29) but could potentially be extended to three-dimensional distributions. STED offers improved axial resolution compared to this form of FPALM, but it is interesting to consider a modified FPALM that uses TIRF or 4Pi (two-photon) excitation to improve axial resolution and confine activation. Such a method would be ideal for studies of membrane protein distributions where lateral resolution is crucial and reduced background (e.g., due to out-of-focus contributions) is highly desirable. Additionally, STED and TIRF could be used in combination to spatially control the excitation profile (13,55). The procedures for velocity and position analysis of large numbers of single molecules ($\sim 10^5$) already developed for use with FSM and TIR-FSM (21,22) could be used to analyze FPALM images as well.

The authors thank Dr. David Clark for the spectrometer, Thomas Tripp for professional machining, and Drs. Joshua Zimmerberg and Paul Blank for the Argon ion laser. Special thanks to Dr. George Bernhardt, Patrick Swinney, and Prof. Scott Collins for production and atomic force microscopy of the sapphire sample for calibration. The authors are grateful to Dr. George Patterson for providing PA-GFP samples and unpublished data.

S.T.H. was supported by National Institutes of Health grant 1-K25-AI65459-01 and startup funds from the Office of the Vice President for Research at the University of Maine.

At the time of publication, a related work by E. Betzig et al. had recently appeared online in the journal *Science* (56).

REFERENCES

1. Alberts, B. 2002. Molecular Biology of the Cell. Garland Science, New York.
2. Richards, B., and E. Wolf. 1959. Electromagnetic diffraction in optical systems. 2. Structure of the image field in an aplanatic system. *Proc. R. Soc. Lond. A Math. Phys. Sci.* 253:358–379.
3. Born, M., and E. Wolf. 1997. Principles of Optics: Electromagnetic Theory of Propagation, Interference and Diffraction of Light. Cambridge University Press, Cambridge, UK.
4. Hell, S. W., M. Schrader, and H. T. van der Voort. 1997. Far-field fluorescence microscopy with three-dimensional resolution in the 100-nm range. *J. Microsc.* 187:1–7.
5. Schrader, M., and S. W. Hell. 1998. Three-dimensional super-resolution with a 4Pi-confocal microscope using image restoration. *J. Appl. Phys.* 84:4033–4042.
6. Hell, S., and E. H. K. Steltzer. 1992. Properties of a 4Pi confocal fluorescence microscope. *J. Opt. Soc. Am. A.* 9:2159–2167.
7. Egner, A., and S. W. Hell. 2005. Fluorescence microscopy with super-resolved optical sections. *Trends Cell Biol.* 15:207–215.
8. Egner, A., S. Jakobs, and S. W. Hell. 2002. Fast 100-nm resolution three-dimensional microscope reveals structural plasticity of mitochondria in live yeast. *Proc. Natl. Acad. Sci. USA.* 99:3370–3375.
9. Egner, A., S. Verrier, A. Goroshkov, H. D. Soling, and S. W. Hell. 2004. 4Pi-microscopy of the Golgi apparatus in live mammalian cells. *J. Struct. Biol.* 147:70–76.
10. Gustafsson, M. G. 2005. Nonlinear structured-illumination microscopy: wide-field fluorescence imaging with theoretically unlimited resolution. *Proc. Natl. Acad. Sci. USA.* 102:13081–13086.
11. Hanser, B. M., M. G. Gustafsson, D. A. Agard, and J. W. Sedat. 2004. Phase-retrieved pupil functions in wide-field fluorescence microscopy. *J. Microsc.* 216:32–48.
12. Klar, T. A., E. Engel, and S. W. Hell. 2001. Breaking Abbe's diffraction resolution limit in fluorescence microscopy with stimulated emission depletion beams of various shapes. *Phys. Rev. E.* 64:066613.
13. Klar, T. A., S. Jakobs, M. Dyba, A. Egner, and S. W. Hell. 2000. Fluorescence microscopy with diffraction resolution barrier broken by stimulated emission. *Proc. Natl. Acad. Sci. USA.* 97:8206–8210.
14. Westphal, V., and S. W. Hell. 2005. Nanoscale resolution in the focal plane of an optical microscope. *Phys. Rev. Lett.* 94:143903.
15. Hofmann, M., C. Eggeling, S. Jakobs, and S. W. Hell. 2005. Breaking the diffraction barrier in fluorescence microscopy at low light intensities by using reversibly photoswitchable proteins. *Proc. Natl. Acad. Sci. USA.* 102:17565–17569.
16. Lacoste, T. D., X. Michalet, F. Pinaud, D. S. Chemla, A. P. Alivisatos, and S. Weiss. 2000. Ultrahigh-resolution multicolor colocalization of single fluorescent probes. *Proc. Natl. Acad. Sci. USA.* 97:9461–9466.
17. Lakowicz, J. R. 1983. Principles of Fluorescence Spectroscopy. Plenum Press, New York.
18. Forster, T. 1948. Zwischenmolekulare Energiewanderung Und Fluoreszenz. *Annalen Der Physik.* 2:55–75.
19. Fung, B. K., and L. Stryer. 1978. Surface density determination in membranes by fluorescence energy transfer. *Biochemistry.* 17:5241–5248.
20. Michalet, X., and S. Weiss. 2006. Using photon statistics to boost microscopy resolution. *Proc. Natl. Acad. Sci. USA.* 103:4797–4798.
21. Ponti, A., M. Machacek, S. L. Gupton, C. M. Waterman-Storer, and G. Danuser. 2004. Two distinct actin networks drive the protrusion of migrating cells. *Science.* 305:1782–1786.
22. Ponti, A., A. Matov, M. Adams, S. Gupton, C. M. Waterman-Storer, and G. Danuser. 2005. Periodic patterns of actin turnover in lamellipodia and lamellae of migrating epithelial cells analyzed by quantitative Fluorescent Speckle Microscopy. *Biophys. J.* 89:3456–3469.
23. Waterman-Storer, C., A. Desai, and E. D. Salmon. 1999. Fluorescent speckle microscopy of spindle microtubule assembly and motility in living cells. *Methods Cell Biol.* 61:155–173.
24. Waterman-Storer, C. M., A. Desai, J. C. Bulinski, and E. D. Salmon. 1998. Fluorescent speckle microscopy, a method to visualize the dynamics of protein assemblies in living cells. *Curr. Biol.* 8:1227–1230.
25. Patterson, G. H., and J. Lippincott-Schwartz. 2002. A photoactivatable GFP for selective photolabeling of proteins and cells. *Science.* 297:1873–1877.
26. Aubry, R., C. Dua, J. C. Jacquet, F. Lemaire, P. Galtier, B. Dessertenne, Y. Cordier, M. A. DiForte-Poisson, and S. L. Delage. 2004. Temperature measurement by micro-Raman scattering spectroscopy in the active zone of AlGaN/GaN high electron-mobility transistors. *Eur. Phys. J. Appl. Phys.* 27:293–296.
27. Thompson, R. E., D. R. Larson, and W. W. Webb. 2002. Precise nanometer localization analysis for individual fluorescent probes. *Biophys. J.* 82:2775–2783.
28. Cheezum, M. K., W. F. Walker, and W. H. Guilford. 2001. Quantitative comparison of algorithms for tracking single fluorescent particles. *Biophys. J.* 81:2378–2388.
29. Albota, M., D. Beljonne, J. L. Bredas, J. E. Ehrlich, J. Y. Fu, A. A. Heikal, S. T. Hess, T. Kogej, M. D. Levin, S. R. Marder, D. McCord-Maughon, J. W. Perry, H. Rockel, M. Rumi, C. Subramaniam, W. W. Webb, X. L. Wu, and C. Xu. 1998. Design of organic molecules with large two-photon absorption cross sections. *Science.* 281:1653–1656.
30. Hess, S. T., A. A. Heikal, and W. W. Webb. 2004. Fluorescence photoconversion kinetics in novel green fluorescent protein pH sSensors. *J. Phys. Chem. B.* 108:10138–10148.

31. Lukyanov, K. A., D. M. Chudakov, S. Lukyanov, and V. V. Verkhusha. 2005. Innovation: photoactivatable fluorescent proteins. *Nat. Rev. Mol. Cell Biol.* 6:885–891.

32. Pawley, J. B. 1995. Handbook of Biological Confocal Microscopy. Plenum Press, New York.

33. Shvartsman, D. E., M. Kotler, R. D. Tall, M. G. Roth, and Y. I. Henis. 2003. Differently anchored influenza hemagglutinin mutants display distinct interaction dynamics with mutual rafts. *J. Cell Biol.* 163:879–888.

34. Sandison, D. R., D. W. Piston, R. M. Williams, and W. W. Webb. 1995. Quantitative comparison of background rejection, signal-to-noise ratio, and resolution in confocal and full-field laser-scanning microscopes. *Appl. Opt.* 34:3576–3588.

35. Sandison, D. R., and W. W. Webb. 1994. Background rejection and signal-to-noise optimization in confocal and alternative fluorescence microscopes. *Appl. Opt.* 33:603–615.

36. Kenworthy, A. K., B. J. Nichols, C. L. Remmert, G. M. Hendrix, M. Kumar, J. Zimmerberg, and J. Lippincott-Schwartz. 2004. Dynamics of putative raft-associated proteins at the cell surface. *J. Cell Biol.* 165:735–746.

37. Lippincott-Schwartz, J., E. Snapp, and A. Kenworthy. 2001. Studying protein dynamics in living cells. *Nat. Rev. Mol. Cell Biol.* 2:444–456.

38. Swaminathan, R., C. P. Hoang, and A. S. Verkman. 1997. Photobleaching recovery and anisotropy decay of green fluorescent protein GFP-S65T in solution and cells: Cytoplasmic viscosity probed by green fluorescent protein translational and rotational diffusion. *Biophys. J.* 72:1900–1907.

39. Peterman, E. J. G., S. Brasselet, and W. E. Moerner. 1999. The fluorescence dynamics of single molecules of green fluorescent protein. *J. Phys.Chem. A.* 103:10553–10560.

40. Schutz, G. J., G. Kada, V. P. Pastushenko, and H. Schindler. 2000. Properties of lipid microdomains in a muscle cell membrane visualized by single molecule microscopy. *EMBO J.* 19:892–901.

41. Fujiwara, T., K. Ritchie, H. Murakoshi, K. Jacobson, and A. Kusumi. 2002. Phospholipids undergo hop diffusion in compartmentalized cell membrane. *J. Cell Biol.* 157:1071–1081.

42. Nakada, C., K. Ritchie, Y. Oba, M. Nakamura, Y. Hotta, R. Iino, R. S. Kasai, K. Yamaguchi, T. Fujiwara, and A. Kusumi. 2003. Accumulation of anchored proteins forms membrane diffusion barriers during neuronal polarization. *Nat. Cell Biol.* 5:626–632.

43. Chalfie, M., and S. Kain. 1998. Green Fluorescent Protein: Properties, Applications, and Protocols. Wiley-Liss, New York.

44. Patterson, G. H., S. M. Knobel, W. D. Sharif, S. R. Kain, and D. W. Piston. 1997. Use of the green fluorescent protein and its mutants in quantitative fluorescence microscopy. *Biophys. J.* 73:2782–2790.

45. Tsien, R. Y. 1998. The green fluorescent protein. *Annu. Rev. Biochem.* 67:509–544.

46. Shaner, N. C., P. A. Steinbach, and R. Y. Tsien. 2005. A guide to choosing fluorescent proteins. *Nat. Methods.* 2:905–909.

47. Kwik, J., S. Boyle, D. Fooksman, L. Margolis, M. P. Sheetz, and M. Edidin. 2003. Membrane cholesterol, lateral mobility, and the phosphatidylinositol 4,5-bisphosphate-dependent organization of cell actin. *Proc. Natl. Acad. Sci. USA.* 100:13964–13969.

48. Zacharias, D. A., J. D. Violin, A. C. Newton, and R. Y. Tsien. 2002. Partitioning of lipid-modified monomeric GFPs into membrane microdomains of live cells. *Science.* 296:913–916.

49. Chan, W. C., D. J. Maxwell, X. Gao, R. E. Bailey, M. Han, and S. Nie. 2002. Luminescent quantum dots for multiplexed biological detection and imaging. *Curr. Opin. Biotechnol.* 13:40–46.

50. Michalet, X., F. F. Pinaud, L. A. Bentolila, J. M. Tsay, S. Doose, J. J. Li, G. Sundaresan, A. M. Wu, S. S. Gambhir, and S. Weiss. 2005. Quantum dots for live cells, in vivo imaging, and diagnostics. *Science.* 307:538–544.

51. Heikal, A. A., S. T. Hess, and W. W. Webb. 2001. Multiphoton molecular spectroscopy and excited-state dynamics of enhanced green fluorescent protein (EGFP): acid-base specificity. *Chem. Phys.* 274: 37–55.

52. Yildiz, A., J. N. Forkey, S. A. McKinney, T. Ha, Y. E. Goldman, and P. R. Selvin. 2003. Myosin V walks hand-over-hand: single fluorophore imaging with 1.5-nm localization. *Science.* 300:2061–2065.

53. Yildiz, A., M. Tomishige, R. D. Vale, and P. R. Selvin. 2004. Kinesin walks hand-over-hand. *Science.* 303:676–678.

54. Chen, Y., P. J. MacDonald, J. P. Skinner, G. H. Patterson, and J. D. Muller. 2006. Probing nucleocytoplasmic transport by two-photon activation of PA-GFP. *Microsc. Res. Tech.* 69:220–226.

55. Cragg, G. E., and P. T. C. So. 2000. Lateral resolution enhancement with standing evanescent waves. *Opt. Lett.* 25:46–48.

56. Betzig, E., G. H. Patterson, R. Sougrat, O. W. Lindwasser, S. Olenych, J. S. Bonifacino, M. W. Davidson, J. Lippincott-Schwartz, and H. F. Hess. 2006. Imaging intracellular fluorescent proteins at nanometer resolution. *Science.* 313:1642–1645.